ChemComm

COMMUNICATION

View Article Online
View Journal | View Issue

Cite this: *Chem. Commun.*, 2023, 59, 11393

Received 20th July 2023,
Accepted 11th August 2023

DOI: 10.1039/d3cc03501h

rsc.li/chemcomm

Nanoporous YVO_4 as a luminescent host for probing molecular encapsulation†

Milena Lima Brito,[a] Steven Huband,[b] Marc Walker,[b] Richard I. Walton[c] and Paulo C. de Sousa Filho*[a]

Control of phase separation of VO_4^{3-} and rare earth precursors in reverse microemulsions afforded ~35 nm YVO_4 nanoparticles with functionalisable ~7 ± 3 nm nanopores. Doping by Eu^{3+} allowed luminescent probing of interfacial crystallisation while xylenol orange absorption showed molecular encapsulation in particle cavities. This provides potential multifunctional systems combining UV-Vis-NIR luminescence and (photo)active molecules for optical sensing.

Strategies for the association of multiple properties in a single structure are a challenge for the development of new cutting-edge nanomaterials.[1] In particular, light-driven responses of nanoparticles, which include thermometry,[2] chemical sensing,[3] and localized activation of chemical reactions,[4] can be combined to afford multiple actions against a local chemical environment.[5] Rare earths (RE) fulfil lifetime, antiphotobleaching, and linewidth requirements for luminescent sensing,[6] and RE vanadates are chemically versatile solids providing both ultraviolet (UV)- and near infrared (NIR)-excited emissions,[7] as well as catalytic potential towards biomimetic reactions.[8] Hollow or nanoporous particles[9] with accessible cavities for functionalisation are promising structures to further improve the range of applications of this class of solids towards multifunctional materials. Engineered cavities can act as nanocontainers for encapsulation and transport of molecules of interest such as dyes and drugs, which can be selectively activated *via* the light emitted by the particles. In turn, these systems offer novel prospects for theranostic applications, where different selected wavelengths can provide orthogonal sensing and photoactivation of encapsulated molecules.[4,10] The synthesis of porous and hollow particles generally follow soft template routes[9] *via* the growth of the inorganic phase over liquid–liquid or liquid–air discontinuities. Regular (*i.e.*, oil-in-water) and reverse (*i.e.*, water-in-oil) microemulsions consist of thermodynamically stable systems providing nanometric liquid–liquid interfaces, which can further enable phase separation of different precursors into polar and non-polar domains for a controlled crystallisation of the inorganic product.[11] Although this has been widely explored to produce hollow metal and oxide nanoparticles,[12] a limited number of examples demonstrate the possibility of functionalisation of the inner surface of RE-based luminescent particles,[13] especially of vanadates. We have therefore investigated the formation of tetragonal $REVO_4$ hollow particles in reverse microemulsions containing separated RE^{3+} and VO_4^{3-} precursors in dodecane and water phases, respectively (ESI,† Section S1 and Fig. S1–S3). We produced Eu^{3+}-doped particles to probe spectroscopically the crystallisation process, and Yb^{3+}/Er^{3+}-doped particles to confirm the potentiality of the products for mutifunctional NIR-excited luminescent sensing.

Considering both size distributions and dynamic light scattering (DLS) polydispersity indices (ESI,† Section S2.1 and Fig. S3), the microemulsions with water/surfactant ratios (W_O, ESI,† Section S1) $W_O = 20$ and $W_O = 25$ induced the interface precipitation of the vanadate phase; $W_O = 25$ was further investigated. The formation kinetics of $REVO_4$ solids from aqueous precursors usually follows a non-classic nucleation/growth mechanism,[14] being strongly dependent on the pH because of vanadate speciation and formation of non-crystalline metastable intermediates. Highly basic pH results in higher concentrations of VO_4^{3-}(aq), but also induces competitive precipitation of kinetically stable RE hydroxides.[14,15] Conversely, acidic metavanadate ($(VO_3)_n^{n-}$) solutions show a smaller availability of free VO_4^{3-} and may lead to the parallel precipitation of polyvanadates.[16]

We therefore evaluated initially the effect of the pH (= 7, 11.5 or 13) of the aqueous cores on the interface crystallization of

[a] *Department of Inorganic Chemistry, Institute of Chemistry, University of Campinas (Unicamp), R. Monteiro Lobato, 270, 13083-970, Campinas, São Paulo, Brazil. E-mail: pcsfilho@unicamp.br*
[b] *Department of Physics, University of Warwick, Gibbet Hill Road, Coventry CV4 7AL, UK*
[c] *Department of Chemistry, University of Warwick, Gibbet Hill Road, Coventry CV4 7AL, UK*

† Electronic supplementary information (ESI) available: Experimental details, additional data, FTIR, TGA, ζ potential, XPS, XRD, Raman, SEM, luminescence, and UV-Vis spectra. See DOI: https://doi.org/10.1039/d3cc03501h

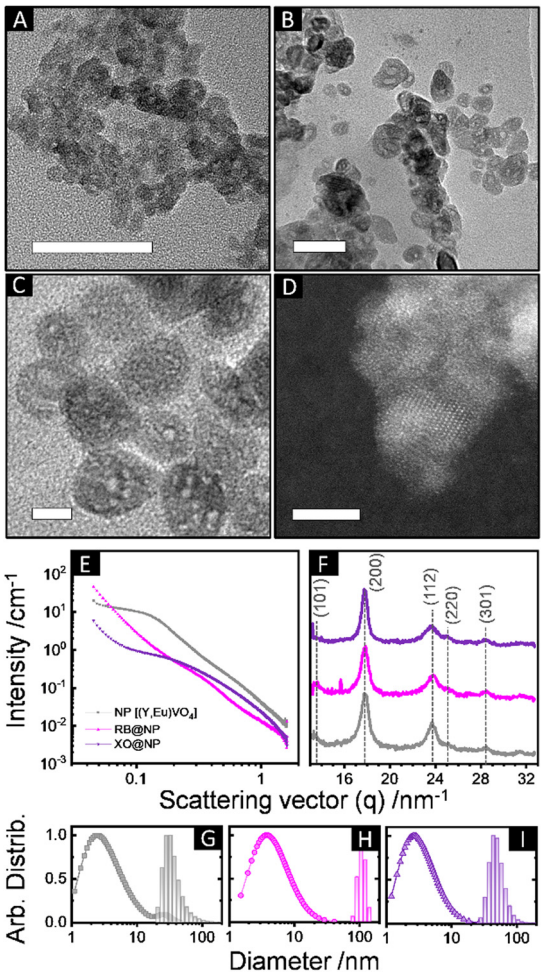

Fig. 1 (A)–(D) Transmission electron microscopy (TEM) images of (Y,Eu)VO_4 nanoparticles synthesised in reverse microemulsions (W_O = 25, pH = 11.5). Scale bars correspond to 50 nm in (A) and (B), 10 nm in (C), and 5 nm in (D, HRTEM). (E) SAXS and (F) WAXS profiles of non-modified (Y,Eu)VO_4 nanoparticles (NP, grey), and particles synthesised at the same conditions containing encapsulated rose Bengal (RB@NP, rose), or xylenol orange (XO@NP, purple) dyes. (G)–(I) Size distributions obtained from SAXS (in volumes, points) and DLS (in number, bars) of (G) NP [SAXS: D_m^{i} = 6.7 ± 2.4 nm, D_m^{ii} = 28 ± 7 nm; DLS: D_H = 34 ± 8 nm, PDI = 0.4], (H) RB@NP [SAXS: D_m = 8.7 ± 3.5 nm; DLS: D_H = 110 ± 15 nm, PDI = 0.86], and (I) XO@NP [SAXS: D_H = 5.8 ± 2.2 nm; DLS: D_H = 51 ± 13 nm, PDI = 0.6]. The colour pattern of (E), (F) was kept for (G)–(I). D_m and D_H stand for mean SAXS-modelled and hydrodynamic (DLS) diameters, respectively, obtained from lognormal fits. SAXS distributions account mostly for the porosity of the particles; DLS distributions refer to hydrodynamic diameters of particles and aggregates in suspension (ESI,† Section S2.2).

$REVO_4$ in reverse microemulsions with W_O = 25 (ESI,† Section S2.1 and Fig. S4). At strongly basic conditions (pH = 13), the reaction mixture containing organic RE oleate precursors and the aqueous vanadate solution remained clear after 80 h. Although the formation of primary grains of tetragonal nanocrystalline (Y,Eu)VO_4 phase could be observed by wide-angle X-ray scattering (WAXS, Fig. S5, ESI†), no solid product was isolated from the reaction mixture. If the pH of the aqueous phase was brought to 7 using $NaVO_3$ as the vanadate source, the particles underwent an uncontrolled growth and only large micrometric aggregates were recovered after 24 h (Fig. S6, ESI†). Therefore, the optimal conditions to assure an interfacial crystallisation of the $REVO_4$ phase in the reverse microemulsions comprised the use of a Na_3VO_4 solution with pH adjusted to 11.5. Such conditions led to the formation of ~35 nm spheroid particles containing multiple cavities (Fig. 1(A)–(D) and Fig. S7, ESI†). The nanoporous nature of the products was probed by small-angle X-ray scattering profiles (SAXS, Fig. 1(E), (G)–(I) and ESI†), which revealed a pore distribution centred at ~5 ± 3 nm. WAXS profiles (Fig. 1(F)) confirmed the formation of tetragonal ($I4_1/amd$) nanocrystallites with (200) coherence lengths of ~7–9 nm. Other characterisation of the particles is shown on the ESI† (Section S2.2). The presence of solvent and surfactant residues that induce partial aggregation in aqueous suspension (Fig. 1(A)–(D), TEM, and Fig. 1(G)–(I), DLS) is confirmed by X-ray photoelectron spectroscopy (XPS, Fig. 2(A)–(D)). The C1s peaks confirmed the presence of high amounts of aliphatic (284.6 eV) and partially oxidised (C–O, C═O, COO, 285.8, 287.0, 288.5 eV) carbon species. Also, minor amounts of carbonates (290.0 eV) were detected due to partial carbonation of the Na_3VO_4 precursor, as observed for $REVO_4$ particles prepared by aqueous coprecipitation.[14,15] The interfacial crystallisation enabled the encapsulation of dye molecules in the particle cavities, which showed no effect on the general morphologic and structural properties of the final $REVO_4$ solids (Fig. 1(E)–(I)) besides an increased degree of aggregation (Fig. 1(G)–(I) and ESI,† Section S2.2). Regarding the $REVO_4$ phase, Y3d and V2p signals (Fig. 2(A) and (C)) showed metal sites with oxygen deficiency, as shown by the side-peaks in the Y3d doublet ($3d_{3/2}$, 159.9 eV and $3d_{5/2}$, 157.9 eV), and by V2p peaks due to V(IV) ($2p_{1/2}$, 524.9 eV, $2p_{3/2}$, 517.7 eV). Compositional analysis of XPS spectra (Fig. 2(D)) showed a high Y/V non-stoichiometry (Y/V = 1.7), attesting that the proposed synthesis afforded (Y,Eu)VO_4 particles with a vanadium-deficient surface because of carbonates and hydroxides,[15] also showing a high density of partially reduced metal sites due to oxygen vacancies. Together these results demonstrate the possibility of preparation of $REVO_4$ nanoparticles in water-in-*n*-dodecane reverse microemulsions formed by nanoaggregates of reverse micelles. The phase separation of RE^{3+} and VO_4^{3-} precursor results in the interfacial crystallisation over these templates upon diffusion of RE oleates and VO_4^{3-} ions along the surfactant film, yielding nanoporous $REVO_4$ particles (Fig. 2(E)). Given the high chemical and structural similarity of RE vanadates, this method can be easily adapted to produce nanoporous particles composed by other lanthanides to offer multiple luminescent properties.

The obtained (Y,Eu)VO_4 particles showed the characteristic $^5D_0 \rightarrow {}^7F_J$ (J = 0–4) Eu^{3+} emissions upon 280 nm excitation due to $^1T_{1,2} \leftarrow {}^1A_1$ absorption followed by $VO_4^{3-} \rightarrow Eu^{3+}$ energy transfer.[7,17] The luminescent intensities and the Eu^{3+}spectral profiles in the oleate precursors and $REVO_4$ products are remarkably different (Fig. S10, ESI†), enabling application of Eu^{3+} luminescence spectroscopy to follow the crystallisation of the $REVO_4$ phase (Fig. 2(F)–(J) and ESI,† Section S2.3). While

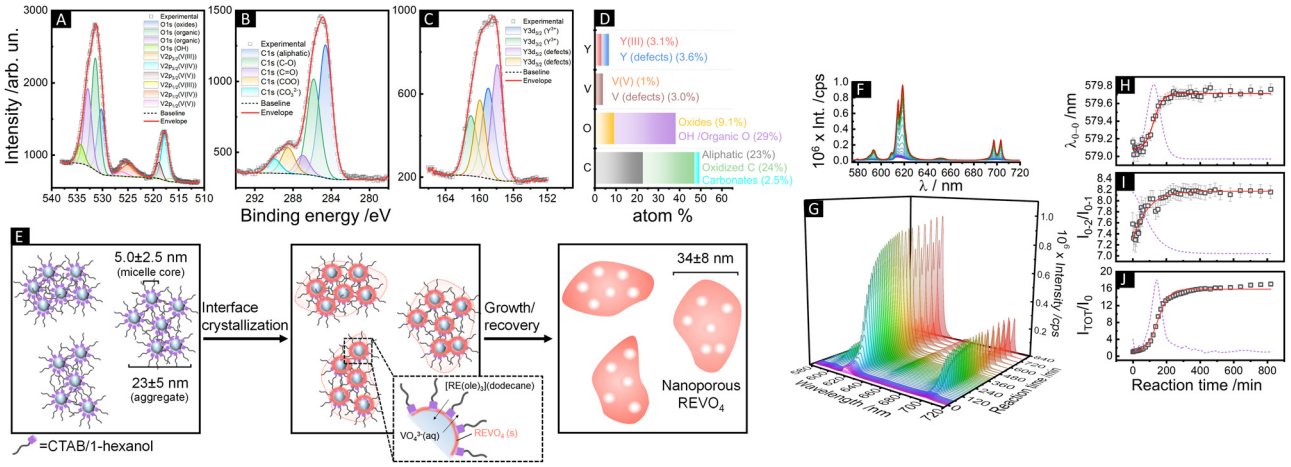

Fig. 2 (A)–(C) XPS spectra of (Y,Eu)VO_4 nanoparticles obtained by reverse microemulsion synthesis (W_O = 25, pH = 11.5) showing the (A) O1s and V2p, (B) C1s, and (C) Y3d peaks. Survey spectra are shown in Fig. S10 (ESI†). (D) Compositional results (% mol) obtained from XPS spectra (Eu and residual Si are not shown for clarity). (E) Schematic illustration of the formation of nanoporous $REVO_4$ particles by interface crystallization over micellar aggregates in water-in-*n*-dodecane reverse microemulsions. (F)–(J) *In situ* luminescence monitoring of the formation of (Y,Eu)VO_4 particles in water-in-*n*-dodecane reverse microemulsions (W_O = 25, 25 °C, pH = 11.5). Emission spectra (λ_{exc} = 288 nm) shown as (F) superposed lines and (G) wavelength *vs.* time *vs.* intensity profiles. (H) Position of the $^5D_0 \rightarrow {}^7F_0$ barycentre (λ_{0-0}), (I) intensity ratio between the $^5D_0 \rightarrow {}^7F_2$ and $^5D_0 \rightarrow {}^7F_1$ transitions (I_{02}/I_{01}), and (J) the total integrated intensity normalised with respect to the integrated intensity at t = 0 (I_{TOT}/I_0). The red solid lines and the dotted violet lines correspond to sigmoidal fits of the experimental data and the respective first derivatives. Kinetic data involving different reaction conditions are shown in ESI† (Section S2.3 and Fig. S12).

the total luminescence intensities (I_{TOT}/I_0) are known to be correlated to the number and crystalline quality of the nanocrystals,[14,18] here we demonstrate that additional qualitative kinetic information can be accessed by the ratio between the Eu^{3+} $^5D_0 \rightarrow {}^7F_2$ and $^5D_0 \rightarrow {}^7F_1$ intensities (I_{02}/I_{01}) and by the barycentre of the $^5D_0 \rightarrow {}^7F_0$ transition (λ_{0-0}), which account for the evolution of microsymmetry around Eu^{3+} ions (ESI,† Section S2.3).

Such parameters reflect the degree of formation of nanocrystals from precursors, as well as amorphous-to-crystalline conversions of intermediates. The luminescence *vs.* time profiles (Fig. 2(F) and (G)) show an initial induction period of low luminescence, followed by a steep increase in intensities due to fast nucleation and growth of nanocrystals. The λ_{0-0} and I_{02}/I_{01} parameters became constant after 280 min of reaction at the optimised conditions (pH = 11.5 and 25 °C), indicating no further alterations of microsymmetry around Eu^{3+} ions after this period (Fig. 2(H) and (I)). Conversely, the total intensities (Fig. 2(J)) still increase at low rates from 280 to 800 min of reaction, which is ascribed to the improvement of the crystalline quality of the particles due to redissolution of smaller grains without significant alteration of the chemical environment around Eu^{3+}.[17] Different conditions of temperature and pH (Fig. S12, ESI†) resulted in weaker Eu^{3+} emissions and led to uncontrolled morphology (pH = 7, 25 °C) or to unrecoverable products with incomplete consumption of precursors (pH = 11.5, 10 °C or pH = 13, 25 °C). The induction times before burst nucleation and growth in the different conditions (shown by logarithmic plots in Fig. S13, ESI†) correspond to the transformation of homogeneous precursors diffusing along the surfactant film to generate pre-nucleation clusters towards the formation of nuclei and nanocrystallites. The increase in the pH of the aqueous phase resulted in a decrease of the induction period from ~100 min (pH = 7) to ~50 min (pH = 11.5) and <10 min (pH = 13.5) due to higher availability of free VO_4^{3-} anions in comparison to protonated (*e.g.*, $H_xVO_4^{(3-x)-}$) or condensed (*e.g.*, $(VO_3)_n^{n-}$) species at high pH.[16] However, at pH = 13 the total intensity starts to decrease after ~60 min, indicating the consumption of the initial RE/VO_4^{3-} clusters and primary grains to form non-luminescent species such as hydroxides or hydroxo complexes. In this case (pH = 13) no evolution of the I_{02}/I_{01} parameter is observed (I_{02}/I_{01} < 7, Fig. S12Q, ESI†), suggesting that most of the RE ions remain as oleates or as kinetically stable hydroxides/hydroxo complexes, and only a minor amount of $REVO_4$ primary grains was formed at the end of the reaction (Fig. S6, ESI†). At pH = 7, vanadate species are mainly present as $(VO_3)_n^{n-}$, and the lower availability of VO_4^{3-} imposes a longer induction period (~100 min) and a slower growth rate (Fig. S12J–N, ESI†). This accounts for the competitive formation of kinetically stable metavanadates (*e.g.*, $RE_n(VO_3)_{3n}$) which are further converted into the $REVO_4$ phase in a slow step. Interestingly, the reaction at low temperature (10 °C, pH = 11.5) resulted in a shorter induction period (10–20 min) in comparison to the room temperature conditions, contrary to the expected behaviour. This can be tentatively ascribed to the preferential concentration of anionic groups of the aqueous phase in the vicinity of the cationic surfactant film due to the reduced thermal diffusion of the solubilizates.

Particles obtained in optimised conditions also showed NIR-excited luminescence despite their rather low processing temperature (Fig. S14, ESI†). Although photon upconversion in high phonon energy (>600 cm^{-1}) lattices is often limited to highly crystalline particles,[19] nanoporous ($Y_{0.78}Yb_{0.20}Er_{0.02}$)$VO_4$ clearly exhibited the characteristic green Er^{3+}

emissions ($^2H_{11/2}$ → $^4I_{15/2}$, 525 nm; $^4S_{3/2}$ → $^4I_{15/2}$, 545 nm) under λ_{exc} = 980 nm,[7] with low contribution of emissions of the $^4F_{9/2}$ state in the red. The Er^{3+}-doped particles changed their emission profile after dispersion in water (Fig. S13B, ESI†), with a reduced contribution of the upper $^2H_{11/2}$ state in comparison to the $^4S_{3/2}$ state. This is possibly due to a laser-induced local self-heating of the particles, which is further confirmed by the linear dependence of the emission intensity ratio of the thermally coupled $^2H_{11/2}$ and $^4S_{3/2}$ states with the pump power (Fig. S14E, ESI†).[20] The bi-logarithmic upconversion power dependence of the Yb^{3+}/Er^{3+} couple showed negative deviations from the expected 2-photon slope ($^2H_{11/5}$: 1.67 ± 0.03; $^4S_{3/2}$: 1.34 ± 0.03, Fig. S13C and D, ESI†), due to the high Yb/Er ratio[21] and to competitive thermal population of $^2H_{11/2}$ and non-radiative relaxation of $^4S_{3/2}$.[20] These results indicate that the Er^{3+}-doped particles not only can provide thermally responsive emissions but also act as localised nanoheaters, with the additional advantage of showing functionalisable nanocavities.

To further demonstrate this possibility, we performed the precipitation reactions in the presence of xylenol orange (XO) and rose Bengal (RB) dyes previously dissolved in the aqueous phase (Fig. 1, ESI,† Sections S1.3 and S2.4). Encapsulated RB was easily removed by washing, but the presence of the dye could be verified by XPS (Fig. S15, ESI†). XO shows a stronger coordination towards RE^{3+} and a pH-responsive absorption, so this dye was used as a probe to attest encapsulation (*i.e.* XO@NP). For comparison, XO was also grafted in equivalent amounts at the external surface (*i.e.* NP@XO Fig. S16–S18, ESI†) of identical (Y,Eu)VO_4 nanoparticles (ESI,† Section S1.3 and S2.4). Even though XO is a pH indicator, NP@XO and XO@NP suspensions in different pHs (3–12) showed no alteration in the absorption profile of the dye (Fig. S17, ESI†), confirming the high affinity of the dye towards the oxide surfaces. After 30 days of exposure (ESI,† Section S2.4, ESI†) at these pHs, XO was partially extracted from the surfaces especially at high pHs, but a more prominent release is observed for the NP@XO system in comparison to XO@NP (Fig. S18 and S19(A)–(B), ESI†). If XO@NP and NP@XO systems are exposed to pH = 11 at 50 °C and ultrasound to force the release of XO, the amount of removed XO is about 10x lower in the first hour of extraction for the encapsulated system, and always lower after 5 washing cycles (Fig. S19(C)–(F), ESI†). This ultimately confirms that for XO@NP the dye molecules are effectively occluded in the cavities of the nanoparticles due to the reverse microemulsion synthesis. Also, low density nature of the particles allowed the removal of the encapsulated dye at controlled conditions, thus enabling us to envisage these systems as nanocontainers for controlled release of different molecules.

In summary, we demonstrated the reverse microemulsion formation of nanoporous $REVO_4$ particles with downshift or upconversion luminescence, with an inner surface that can be functionalised with dye molecules. Luminescence spectroscopy combined to multiple techniques was used as a tool to probe the interfacial crystallisation, and the use of dyes confirmed the possibility of molecule encapsulation for further development of new multifunctional systems for luminescent sensing. We thank CAPES, CNPq (405048/2021-1, 310654/2022-0), FAEPEX, and FAPESP (2022/03442-3, 2018/08334-9), and University of Warwick for funding and access to instrumentation. We also thank CA-IQSC-USP and LNNano/CNPEM for TEM.

Conflicts of interest

There are no conflicts to declare.

Notes and references

1 (*a*) A. Skripka, D. Mendez-Gonzalez, R. Marin, E. Ximendes, B. del Rosal, D. Jaque and P. Rodrígues-Sevilla, *Nanoscale Adv.*, 2021, **3**, 6310–6329; (*b*) B. R. Smith and S. S. Gambhir, *Chem. Rev.*, 2017, **117**, 901–986.
2 S. Premcheska, M. Lederer and A. M. Kaczmarek, *Chem. Commun.*, 2022, **58**, 4288–4307.
3 W. Deng and E. M. Goldys, *Analyst*, 2014, **139**, 5321–5334.
4 (*a*) Z. Zhang, M. K. G. Jayakumar, X. Zheng, S. Shikha, Y. Zhang, A. Bansal, D. J. J. Poon, P. L. Chu, E. L. L. Yeo, M. L. K. Chua, S. K. Chee and Y. Zhang, *Nat. Commun.*, 2019, **10**, 1–12; (*b*) M. Tang, X. Zhu, Y. Zhang, Z. Zhang, Z. Zhang, Q. Mei, J. Zhang, M. Wu, J. Liu and Y. Zhang, *ACS Nano*, 2019, **13**, 10405–10418.
5 J. Krämer, R. Kang, L. M. Grimm, L. De Cola, P. Picchetti and F. Biedermann, *Chem. Rev.*, 2022, **122**, 3459–3636.
6 (*a*) G. Lin and D. Jin, *ACS Sens.*, 2021, **6**, 4272–4282; (*b*) G. Sun, Y. Xie, L. Sun and H. Zhang, *Nanoscale Horiz.*, 2021, **6**, 766–780.
7 R. V. Perrella and P. C. de Sousa Filho, *Dalton Trans.*, 2020, **49**, 911–922.
8 N. Singh, S. K. NaveenKumar, M. Geethika and G. Mugesh, *Angew. Chem., Int. Ed.*, 2021, **60**, 3121–3130.
9 S. F. Soares, T. Fernandes, A. L. Daniel da Silva and T. Trindade, *Proc. R. Soc. A*, 2019, **475**, 20180677.
10 X. Wei, H. Chen, H. P. Tham, N. Zhang, P. Xing, G. Zhang and Y. Zhao, *ACS Appl. Nano Mater.*, 2018, **1**, 3663–3672.
11 A. K. Ganguli, A. Ganguly and S. Vaidya, *Chem. Soc. Rev.*, 2010, **39**, 474–485.
12 S. Wolf and C. Feldmann, *Angew. Chem., Int. Ed.*, 2016, **55**, 15728–15752.
13 (*a*) J. Jung-König, M. Sanhaji, R. Popescu, C. Seidl, E. Zittel, U. Schepers, D. Gerthsen, I. Hilger and C. Feldmann, *Nanoscale*, 2017, **9**, 8362–8372; (*b*) M. Wang, Y. Zhang, M. Ng, A. Skripka, T. Cheng, X. Li, K. K. Bhakoo, A. Y. Chang, F. Rosei and F. Vetrone, *Chem. Sci.*, 2020, **11**, 6653–6661.
14 (*a*) B. Fleury, M. A. Neouze, J. M. Guigner, N. Menguy, O. Spalla, T. Gacoin and D. Carriere, *ACS Nano*, 2014, **8**, 2602–2608; (*b*) M. A. Neouze, A. P. Freitas, R. K. Ramamoorthy, R. Mohammedi, E. Larquet, S. Tusseau-Nenez, D. Carrière and T. Gacoin, *Langmuir*, 2020, **36**, 9124–9131; (*c*) A. P. Freitas, R. K. Ramamoorthy, M. Durelle, E. Larquet, I. Maurin, F. Testard, C. Chevallard, T. Gacoin and D. Carriere, *Nano Lett.*, 2022, **22**, 29–35.
15 R. V. Perrella, M. Walker, T. W. Chamberlain, R. I. Walton and P. C. de Sousa Filho, *Nano Lett.*, 2022, **22**, 3569–3575.
16 D. C. Crans and A. S. Tracey, in *Vanadium Compounds: Chemistry, Biochemistry, and Therapeutic Applications*, ed. A. S. Tracey and D. C. Crans, ACS, Washington D.C., 1998, ACS Symposium Series, vol. 711, ch. 1, pp. 2–29.
17 (*a*) G. Guida, S. Huband, M. Walker, R. I. Walton and P. C. de Sousa Filho, *Nanoscale*, 2021, **13**, 4931–4945; (*b*) K. Binnemans, *Coord. Chem. Rev.*, 2015, **295**, 1–45.
18 G. Schwartz, U. Hananel, L. Avram, A. Goldbourt and G. Markovich, *J. Am. Chem. Soc.*, 2022, **144**, 9451–9457.
19 A. Nadort, J. Zhao and E. M. Goldys, *Nanoscale*, 2016, **8**, 13099–13130.
20 A. H. Li, Z. J. Sun and Q. Lü, *J. Nanopart. Res.*, 2013, **15**, 1–10.
21 V. T. Vera, D. M. Gonzalez, D. J. R. Ramos, A. Igalla, M. Laurenti, R. C. Caceres, E. L. Cabarcos, E. Díaz and J. R. Retama, *J. Mater. Chem. C*, 2021, **9**, 8902–8911.

